ORIGINAL PAPER

A mathematical model of nanoparticulate mixed oxide pseudocapacitors; part I: model description and particle size effects

Hossein Farsi · Fereydoon Gobal

Abstract A mathematical model was developed to describe the performance of nanoparticulate mixed oxide pseudocapacitors based on RuO_2–MO_2 (M being another suitable transition metal) under galvanostatic charge/discharge regime. Both double layer and faradaic processes were taken into account. The effects of the active material's particle size and composition were examined. Furthermore, the influence of discharge current on the extents of double layer and faradaic contributions was analyzed. The model analysis showed that the energy density declined upon increasing the volume fraction of larger particles.

Keywords Pseudocapacitors · Nanoparticles · Metal oxide · Ragone plot · Discharge curve

Nomenclature

A	geometric area of the electrode (cm^2)
C_{dl}	DL capacitance per unit surface area (F cm^{-2})
C_{tot}	total available charge per electrode area (C cm^{-2})
d_{Ru}	diameter of the $RuO_2 \cdot xH_2O$ particles (cm)
d_M	diameter of the $MO_2 \cdot yH_2O$ particles (cm)
E	local electrode potential, $\varphi_2 - \varphi_1$ (V)

H. Farsi (✉)
Department of Chemistry, University of Birjand,
P.O. Box: 97175-615, Birjand, Iran
e-mail: hofarsi@birjand.ac.ir

F. Gobal
Department of Chemistry, Sharif University of Technology,
P.O. Box: 11365-9516, Tehran, Iran
e-mail: gobal@sharif.ir

E_0	initial local electrode potential (V)
f	$\frac{F}{RT}$ (V^{-1})
F	Faraday's constant (96,487 C/equiv)
h_{Ru}	length of crystal lattice on the $RuO_2 \cdot xH_2O$ surface (cm)
h_M	length of crystal lattice on the $MO_2 \cdot yH_2O$ surface (cm)
$i_{0, Ru}$	exchange current density for the faradaic reaction of $RuO_2 \cdot xH_2O$ (A cm^{-2})
$i_{0, M}$	exchange current density for the faradaic reaction of $MO_2 \cdot yH_2O$ (A cm^{-2})
i_1	superficial current density in the matrix phase (A cm^{-2})
i_2	superficial current density in the electrolyte phase (A cm^{-2})
i_C	DL current per unit volume of electrode (A cm^{-3})
i_{cell}	cell current density (A cm^{-2})
I_{cell}	cell current (A)
i_f	faradaic current per unit volume of electrode (A cm^{-3})
$j_{f, Ru}$	faradaic current density of $RuO_2 \cdot xH_2O$ (A cm^{-2})
$j_{f, M}$	faradaic current density of $MO_2 \cdot yH_2O$ (A cm^{-2})
$\bar{i}_c$	dimensionless DL current ($i_c L/i_{cell}$)
$\bar{i}_{cell}$	dimensionless cell current ($i_{cell} L(\kappa_P + \sigma)/\kappa_P \sigma V_0$)
$\bar{i}_f$	dimensionless faradaic current ($i_f L/i_{cell}$)
L	thickness of the electrode, $L = L_+ = L_-$ (cm)
L_A	Avogadro's number (6.0226×10^{23} mol^{-1})
L_S	thickness of the separator (cm)
Q_f	faradaic charge per unit volume of the electrode (C cm^{-3})
$Q_{f, oxd}$	faradaic charge per unit volume of the fully oxidized electrode (C cm^{-3})
$Q_{f, red}$	faradaic charge per unit volume of the fully reduced electrode (C cm^{-3})

R	universal gas constant (8.3143 J mol^{-1} K^{-1})	τ	DL time constant (s)
RAV	relative available charge	ξ	dimensionless position coordinate $\left(\frac{x}{L}\right)$
S_V	specific surface area per unit volume of the electrode (cm^2/cm^3)		
$S_{V,\,Ru}$	contribution of RuO$_2$·xH$_2$O in S_V (cm^2/cm^3)		
$S_{V,\,M}$	contribution of MO$_2$·yH$_2$O in S_V (cm^2/cm^3)		
t	time (s)		
t_d	discharge time (s)		
T	temperature (K)		
U_{Ru}	equilibrium potential for the faradaic reaction of RuO$_2$·xH$_2$O (V) [vs. SCE]		
U_M	equilibrium potential for the faradaic reaction of MO$_2$·yH$_2$O (V) [vs. SCE]		
V_{cell}	volume of the cell (cm^3)		
V_0	initial potential before charge (0.5 V) [vs. SCE]		
x	position coordinate (cm)		
X_M	volume fraction of MO$_2$·yH$_2$O in the electrode		

Greek

$\alpha_{a,\,Ru}$	anodic transfer coefficient of the faradaic reaction of RuO$_2$·xH$_2$O
$\alpha_{a,\,M}$	anodic transfer coefficient of the faradaic reaction of MO$_2$·yH$_2$O
$\alpha_{c,\,Ru}$	cathodic transfer coefficient of the faradaic reaction of RuO$_2$·xH$_2$O
$\alpha_{c,\,M}$	cathodic transfer coefficient of the faradaic reaction of MO$_2$·yH$_2$O
δ_{Ru}	state of charge of RuO$_2$·xH$_2$O
δ_M	state of charge of MO$_2$·yH$_2$O
ε	electrode's porosity
ε_S	separator's porosity
φ_1	potential in the solid matrix phase (V)
φ_2	potential in the electrolyte phase (V)
φ_{ave}	average cell potential (V)
Φ_{cell}	cell potential or the matrix potential difference between the two current collectors (V)
$\overline{\Phi}_{cell}$	dimensionless cell potential $\left(\frac{\Phi_{cell}}{2V_0}\right)$
κ_0	Ionic conductivity of the bulk electrolyte (S cm^{-1})
κ_p	ionic conductivity of the electrolyte inside the pores of the electrode (S cm^{-1})
κ_S	ionic conductivity of the electrolyte inside the pores of the separator (S cm^{-1})
θ	fraction of oxidized species in the faradaic reaction
θ_{Ru}	fraction of oxidized form of RuO$_2$·xH$_2$O in the faradaic reaction
θ_M	fraction of oxidized form of MO$_2$·yH$_2$O in the faradaic reaction
σ	electronic conductivity of the solid matrix phase (S cm^{-1})

Introduction

Supercapacitors are receiving increasing attention due to their higher energy and power densities compared to capacitors and batteries, respectively [1]. Supercapacitors rely on two mechanisms for the accumulation of energy, double layer charging and faradaic processes. Many transition metal oxides, RuO$_2$ [2–6], MnO$_2$ [7–10], CoO$_x$ [11, 12], NiO$_x$ [12, 13], and IrO$_x$ [14], of high surface areas have been employed as the active materials, while RuO$_2$ has received most attention. However, because it is expensive and poisonous, a number of attempts have been made to at least partially substitute RuO$_2$ with other transition metals, such as TiO$_2$–RuO$_2$ [14], NiO–RuO$_2$ [15], RuO$_2$–SnO$_2$ [16], or CrO$_x$–RuO$_2$ [17]. Furthermore, composites containing two metal oxides/hydroxides [18–23], metal oxides and carbonaceous materials [24–26], and metal oxides and conducting polymers [27–28] to modify the electrochemical and structural properties of metal oxides have been reported. However, no model has been developed to explain or rationalize the performance of mixed oxide-based supercapacitors. As for single oxide (and in mixture with active carbon), Lin et al. [29, 30] have developed a model that considers both double layer and faradaic contributions. Their model was analyzed theoretically by the present authors, and factors influencing the performance of supercapacitors are categorized in three classes [31]. Furthermore, the model has been further improved in the light of the packing and concentrated solution theories [32, 33]. Kim and Popov [34] have added the contribution of proton diffusion in and out of the lattice structure in the charge/discharge processes. To the best of our knowledge no mathematical model has been developed to rationalize the performance of mixed oxide based pseudocapacitors.

The purpose of the present work is to develop a model to rationalize the performance of a model mixed oxide supercapacitor considering both double layer and faradaic contributions. The influences of three classes of factors, structural (particle or crystal size, and composition), intrinsic (unit cell lengths and exchange current densities), and operating (cell current) factors, on the performance of model mixed oxide supercapacitor have been analyzed. At this early stage of model development, we have also made the following assumptions: (1) The diffusion of proton into the lattice structures accompanying redox processes have been ignored. (2) The concentration distribution of electrolyte in the pore structure of the active materials has been ignored. (3) Each metal oxide individually shows faradaic capacitance. (4) Temperature is constant and set at room temperature. (5) There are no side chemical/electrochemical reactions.
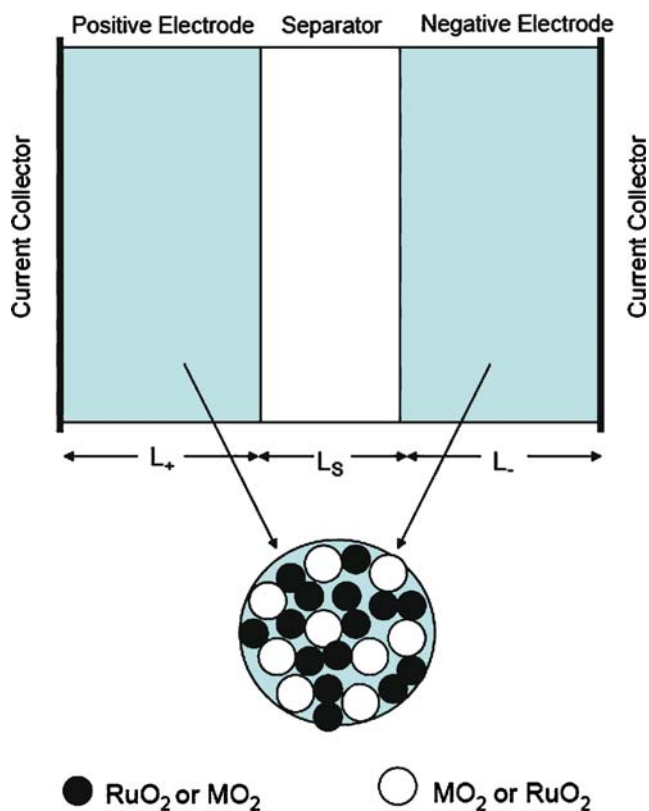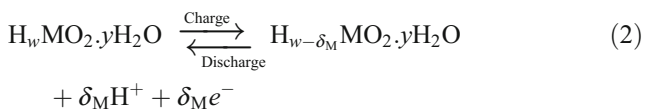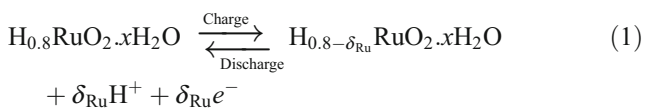
Fig. 1 Schematic presentation of a mixed oxide pseudocapacitor cell in which its composite electrodes contain solid spherical nanoparticles of two different types of metal oxides

Materials and methods

Model description

Figure 1 schematically presents a model supercapacitor with the electrodes based on $RuO_2 \cdot xH_2O$ and $MO_2 \cdot yH_2O$ mixtures placed in 30% sulfuric acid solution and separated by a porous glass separator. The redox processes in the charge/discharge processes of the capacitor at the positive electrode are

$$H_{0.8}RuO_2 \cdot xH_2O \underset{\text{Discharge}}{\overset{\text{Charge}}{\rightleftarrows}} H_{0.8-\delta_{Ru}}RuO_2 \cdot xH_2O \qquad (1)$$
$$+ \delta_{Ru}H^+ + \delta_{Ru}e^-$$

$$H_w MO_2 \cdot yH_2O \underset{\text{Discharge}}{\overset{\text{Charge}}{\rightleftarrows}} H_{w-\delta_M}MO_2 \cdot yH_2O \qquad (2)$$
$$+ \delta_M H^+ + \delta_M e^-$$

with the reverse processes occurring on the negative electrode. Equations 1 and 2 show the faradaic reactions that take place on the surfaces of hydrated RuO_2 and MO_2 particles, respectively. The 0.8 indices are the amount of hydrogen inserted into RuO_2 and comes from Jow and Zheng's [3] work. δ_{Ru}, the state of charge of RuO_2, is the number of proton transferred during charge/discharge process

where Jow and Zheng [3] showed it is equal to 0.5 in the range of 0 to 1 V SCE. There are no experimental results for other metal oxides, but to generalize our model, we consider w and δ_M for the hydrogen inserted amount and the state of charge of MO_2, respectively. This assumption surely does not decisively influence the modeling and can be replaced by the experimental data when these become available.

In this study, it is assumed that both oxides are non-porous spherical particles with uniform size distribution but not necessarily of the same size. The packing theory [31, 33] is used to work out the porosity, ε, in packs of two differently sized spherical particles. The surface area per unit volume of the system, S_V, is then:

$$S_V = 6(1-\varepsilon)\left(\frac{1-X_M}{d_{Ru}} + \frac{X_M}{d_M}\right) \qquad (3)$$

or simply

$$S_V = S_{V,Ru} + S_{V,M} \qquad (4)$$

where d_{Ru} and d_M are the diameters of the Ru and M oxide particles, respectively, and X_M is the volume fraction of $H_w MO_2 \cdot yH_2O$. $S_{V,Ru}$ and $S_{V,M}$ refer to the specific surface area per unit volume contributed by Ru and M oxides, respectively. In line with the packing theory, volume fractions (instead of mole fraction) had to be employed. Because both metal oxides participate in charge transfer reaction, we use S_V as the total specific surface area of unit volume for both double layer charging and faradaic processes.

Governing equations

There are two paths for current passage: the metal oxides matrix, i_1, and the electrolyte phase, i_2 [35]. To derive the variation of the cell potential with time, the amount of charge accumulated, and the energy stored in the capacitor as the functions of the mentioned parameters, we start with the general equation:

$$\frac{\partial i_2}{\partial x} = S_V C_{dl}\left(\frac{\partial(\varphi_2 - \varphi_1)}{\partial t}\right) + S_{V,Ru}j_{f,Ru} + S_{V,M}j_{f,M} \qquad (5)$$

where i_2 is the projected superficial current density to the electrode surface, C_{dl} is the double layer capacitance, φ_1 and φ_2 are potentials in the electrode and electrolyte, respectively, and x is position coordinate. It is clear that φ_2 is zero at $x=0$, the surface of current collector. $j_{f,Ru}$ and $j_{f,M}$ are the faradaic current contributions of Ru and M oxides, respectively, and are derived from the Butler–Volmer equation [36]:

$$j_{f,Ru} = i_{0,Ru}\{\exp[\alpha_{a,Ru}f(E - U_{Ru})] - \exp[-\alpha_{c,Ru}f(E - U_{Ru})]\} \qquad (6)$$

$$j_{f,M} = i_{0,M}\{\exp[\alpha_{a,M}f(E - U_M)] - \exp[-\alpha_{c,M}f(E - U_M)]\} \qquad (7)$$

where $i_{0,\,Ru}$ and $i_{0,\,M}$ are the exchange current densities of the related faradaic reactions, $f = \frac{F}{RT}$, F is Faraday's constant, R is universal gas constant, T is the absolute temperature, and α_a and α_c are the anodic and cathodic transfer coefficients for the reactions, respectively. E, the local electrode potential, is $E = \varphi_2 - \varphi_1$. U_{Ru} and U_M are the equilibrium potentials for reactions 1 and 2, respectively. The fraction of the oxidized surface and the charge are intimately related through:

$$\theta = \frac{Q_f - Q_{f,\text{red}}}{Q_{f,\text{oxd}} - Q_{f,\text{red}}} \tag{8}$$

where $Q_{f,\text{ord}}$ and $Q_{f,\text{red}}$ are the faradaic charges accumulated per unit volume of the electrode at the complete oxidized and reduced states and Q_f is the faradaic charge on the electrode. $Q_{f,\text{red}}$ is assumed zero, and one has:

$$Q_{f,\text{oxd}} = \frac{6(1-\varepsilon)F}{L_A}\left[\frac{1-X_M}{d_{Ru}} \cdot \frac{\delta_{Ru}}{h_{Ru}^2} + \frac{X_M}{d_M} \cdot \frac{\delta_M}{h_M^2}\right] \tag{9}$$

where L_A is the Avogadro number, h_{Ru} and h_M are the unit cell lengths of Ru and M oxides, respectively, that in a sense signify the upper limit of the surface charge density. This equation also points to the contributions of Ru and M oxides in charge accumulation. In terms of θ, one then has:

$$\theta = (1 - X_M)\theta_{Ru} + X_M\theta_M \tag{10}$$

where θ_{Ru} and θ_M are oxidize fraction of Ru and M oxides, respectively. On the other hand,

$$\frac{\partial Q_f}{\partial t} = S_{V,Ru}j_{f,Ru} + S_{V,M}j_{f,M} \tag{11}$$

which relates the extent of charge accumulation to the faradaic currents. Using Eqs. 8 to 11, we arrive at:

$$\frac{\partial \theta_{Ru}}{\partial t} = \frac{L_A h_{Ru}^2}{\delta_{Ru}F}j_{f,Ru} \tag{12}$$

$$\frac{\partial \theta_M}{\partial t} = \frac{L_A h_M^2}{\delta_M F}j_{f,M} \tag{13}$$

$$\frac{\partial \theta}{\partial t} = (1 - X_M)\frac{\partial \theta_{Ru}}{\partial t} + X_M\frac{\partial \theta_M}{\partial t} \tag{14}$$

Jow and Zheng [3] have shown experimentally that, for positive electrode, θ_{Ru} and U_{Ru} are linearly related through:

$$U_{Ru} = 0.5(1 + \theta_{Ru}) \tag{15}$$

For the positive electrode and, similarly, for the negative electrode, one has:

$$U_{Ru} = 0.5\theta_{Ru} \tag{16}$$

There are similar relations for the other oxide, namely:

$$U_M = 0.5(1 + \theta_M) \tag{17}$$

$$U_M = 0.5\theta_M \tag{18}$$

for both the positive and negative electrodes, respectively. These equations show the linear relation between oxidize fractions and potential and, consequently, the amount of charge transferred (the state of charges). In fact, this linear relation gives rise to a rectangular-shaped cyclic voltammogram for pseudocapacitors. The difference between Ru and M oxides is in relation between their state of charge and their oxidized fraction of the active materials. At the same oxidized fraction, the larger the state of charge, the higher the capacity. Therefore, it is conceivable that the M oxide has a lower state of charge value compared to RuO_2 in fully a oxidize state. Jow and Zheng showed that the relation between the state of charge and oxidized fraction of RuO_2 is:

$$\delta_{Ru} = 0.5\theta_{Ru} \tag{19}$$

It means that, for two molecules of RuO_2, only one H^+ ion is adsorbed. For M oxide, similarly,

$$\delta_M = \omega\theta_M \tag{20}$$

Because of the lower capacity of M oxide compared to RuO_2, we expect $\omega < 0.5$.

Assuming that the Ohm's law is obeyed in both the electrode and electrolyte, one has:

$$i_1 = -\sigma_{\text{eff}}\frac{\partial \varphi_1}{\partial x} \tag{21}$$

$$i_2 = -\kappa_p\frac{\partial \varphi_2}{\partial x} \tag{22}$$

with σ_{eff} and κ_p being specific conductivities of the electrode matrix and the electrolyte inside the pores, respectively. κ_p can be calculated by $\kappa_p = \kappa_0\varepsilon^{1.5}$ [35]. The conservation of charge:

$$\frac{\partial i_1}{\partial x} + \frac{\partial i_2}{\partial x} = 0 \tag{23}$$

along with Eqs. 5, 21, and 22 give rise to

$$\frac{\partial^2 E}{\partial \xi^2} = \tau\frac{\partial E}{\partial t} + \frac{L^2}{E_0}\left(\frac{1}{\sigma_{\text{eff}}} + \frac{1}{\kappa_p}\right)$$
$$\times \left(S_{V,Ru}j_{f,Ru} + S_{V,M}j_{f,M}\right) \tag{24}$$

where τ being the time constant of double layer capacitance charging and is of the form:

$$\tau = L^2\left(\frac{1}{\sigma_{\text{eff}}} + \frac{1}{\kappa_p}\right)S_V C_{\text{dl}} \tag{25}$$

In this equation, L is the thickness of one electrode ($L = L_+ = L_-$), and ξ is the reduced distance variable as defined by

$$\xi = \frac{x}{L} \tag{26}$$

Hereafter, the notation "–" shows the dimensionless quantities. Assuming no electronic conductivity for the separator:

$$i_1 = 0 \tag{27}$$

and

$$\frac{\partial i_2}{\partial x} = 0 \tag{28}$$

with

$$i_2 = -\kappa_s \frac{\partial \varphi_2}{\partial x} \tag{29}$$

where κ_s is the ionic conductivity of electrolyte inside the pores of the separator given by $\kappa_s = \kappa_0 \varepsilon^{1.5}$ [35]. To solve the partial differential equation, the following boundary conditions:

at $\xi = 1$, $t > 0$ $\dfrac{\partial E}{\partial \xi} = -\dfrac{i_{cell} L}{E_0 \sigma_{eff}}$ $\qquad$ (30)

at $\xi = 0$, $t > 0$ $\dfrac{\partial E}{\partial \xi} = -\dfrac{i_{cell} L}{E_0 \kappa_p}$ $\qquad$ (31)

$$\frac{\partial \theta_{Ru}}{\partial \xi} = 0 \qquad \frac{\partial \theta_M}{\partial \xi} = 0 \tag{32}$$

and the initial values:

at $t = 0$ for charging; $E = V_0$, $\theta_{Ru} = 0$, $\theta_M = 0$ $\quad$ (33)

at $t = 0$ for discharging;

$$E = 2V_0, \ \theta_{Ru} = 1, \ \theta_M = 1 \tag{34}$$

are imposed. $V_0 = 0.5$ V/SCE for the cell operating between 0 and 1, volt has been assumed. Similar initial and boundary values can be set for the negative electrode. However, as we deal with symmetric cells, the modeling of the positive electrode is carried out only. Using dimensionless potential as defined by $\overline{\varphi}_2 = \frac{\varphi_2}{E_0}$ where $E_0 = 2$ V_0; Eq. 24 simplified to:

$$\frac{\partial^2 \overline{\varphi}_2}{\partial \xi^2} + \frac{1}{\left(1 + \kappa_p/\sigma_{eff}\right)} \frac{\partial^2 \overline{E}}{\partial \xi^2} = 0 \tag{35}$$

with the boundary conditions:

at $\xi = 0, t > 0; \overline{\varphi}_2 = 0$ $\qquad$ (36)

at $\xi = 1, t > 0; \dfrac{\partial \overline{\varphi}_2}{\partial \xi} = \dfrac{i_{cell} L}{E_0 \kappa_p}$ $\qquad$ (37)

and the initial value:

at $t = 0;$ $\overline{\varphi}_2 = 0$ $\qquad$ (38)

The dimensionless potential difference across the terminals of the supercapacitor or dimensionless cell potential, $\overline{\Phi}_{cell}$, is given by:

$$\overline{\Phi}_{cell} = 2\left[\overline{E}\big|_{\xi=0} - \overline{V}_0\right] - 2\left[\overline{\varphi}_2\big|_{\xi=1} - \overline{\varphi}_2\big|_{\xi=0}\right] - \frac{i_{cell} L_S}{E_0 \kappa_S} \tag{39}$$

and the double layer and faradaic contributions to the cell's current are:

$$i_C = -S_V C_{dl} \frac{\partial E}{\partial t} \tag{40}$$

$$i_f = -\left(S_{V,Ru} j_{f,Ru} + S_{V,M} j_{f,M}\right) \tag{41}$$

Another quantity of interest is the relative available charge, RAC, defined as:

$$RAC = \frac{i_{cell} t}{C_{total}} \tag{42}$$

where C_{total} is the total charge accumulated per unit area of the electrode and can be attained through:

$$C_{total} = L\left[\frac{S_{V,Ru} \delta_{Ru} F}{h_{Ru}^2 L_A} + \frac{S_{V,M} \delta_M F}{h_M^2 L_A} + C_{dl} S_V (E_0 - V_0)\right]_{x=1} \tag{43}$$

We have employed backward finite difference method through BAND(j) algorithm [35] in a MatLab environment [37] and linearized the exponential term basically similar to the method used by Lin et al. [29] to solve differential equations 35 and 24. One hundred and three spaces and 4,001 time slots have been used [31], and it was observed that no further improvements were observed upon any increase in the number of space and time slots.

Results and discussion

In this work, we study the effect of nanoparticle size on the performance of the supercapacitor. Therefore, we assumed the same i_0 and h values for both metal oxides. It means that we consider one type of active spherical material of two different nanoparticle sizes, i.e., M≡Ru. In fact, this special case can help us to have a better picture of the effect of particle size distribution on the performance of the supercapacitor. The porosity and, therefore, the specific surface area of mixtures of two spherical nanoparticles will then be a function of both the ratio of the diameters of their constituents as well as their composition, Fig. 2a and b. The porosity values have been calculated through the packing theory, and it passes through a minimum with increasing the volume fraction of M oxide that itself depends to the ratio of $\frac{d_M}{d_{Ru}}$ [32]. Furthermore, S_V increases as the volume fraction of smaller nanoparticles is raised.

Figures 3 and 4 presents the discharge characteristics of two series of capacitors where the only difference is the $\frac{d_M}{d_{Ru}}$ ratios, which are 0.33 and 2, respectively. Table 1 shows the numerical values of model parameters that are used in this simulation. As these figures show discharge time increases as the volume fraction of smaller nanoparticles is increased. This is because of their larger surface area of unit volume, S_V, and thus their larger available charge. Removing of a larger amount of charge obviously takes longer time when starting with the same state of charge.

In Figs. 3a,b and 4a,b, a dramatic slope change that signifies the change in the mechanism of discharge has been observed at the early stages of discharge. The region that the change occurs certainly depends on the cell current and shifts to lower cell potential as the cell current increases. This points to the larger overpotentials encoun-
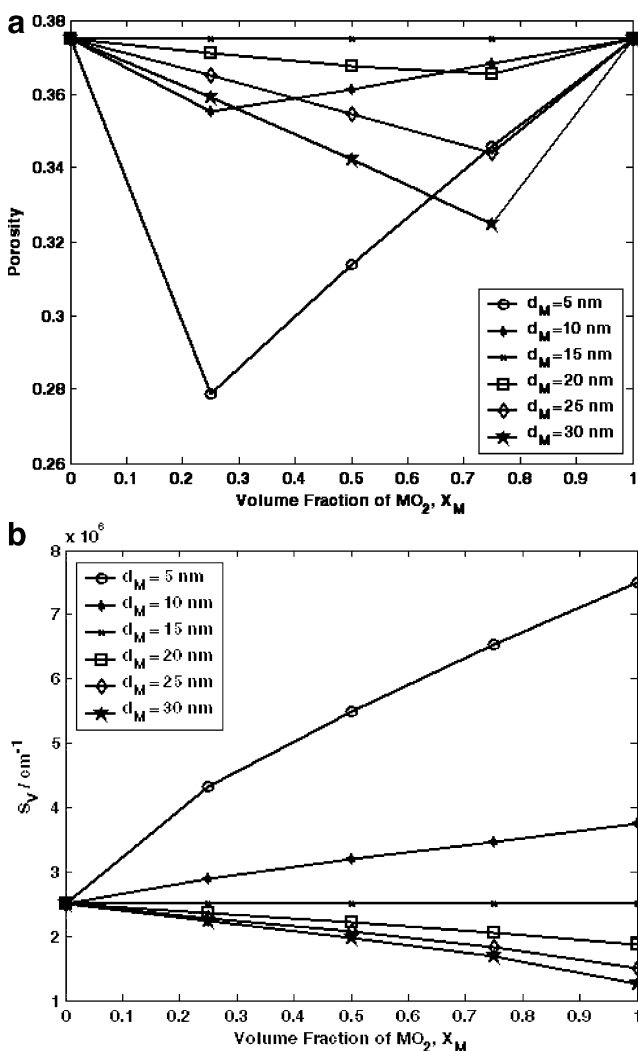

Fig. 2 The profile of porosity (a) and specific surface area per unit volume of the electrode (b) vs. volume fraction of MO_2 via packing theory. The MO_2 nanoparticles have different sizes as shown in the legend, while the size of RuO_2 nanoparticles is fixed at 15 nm
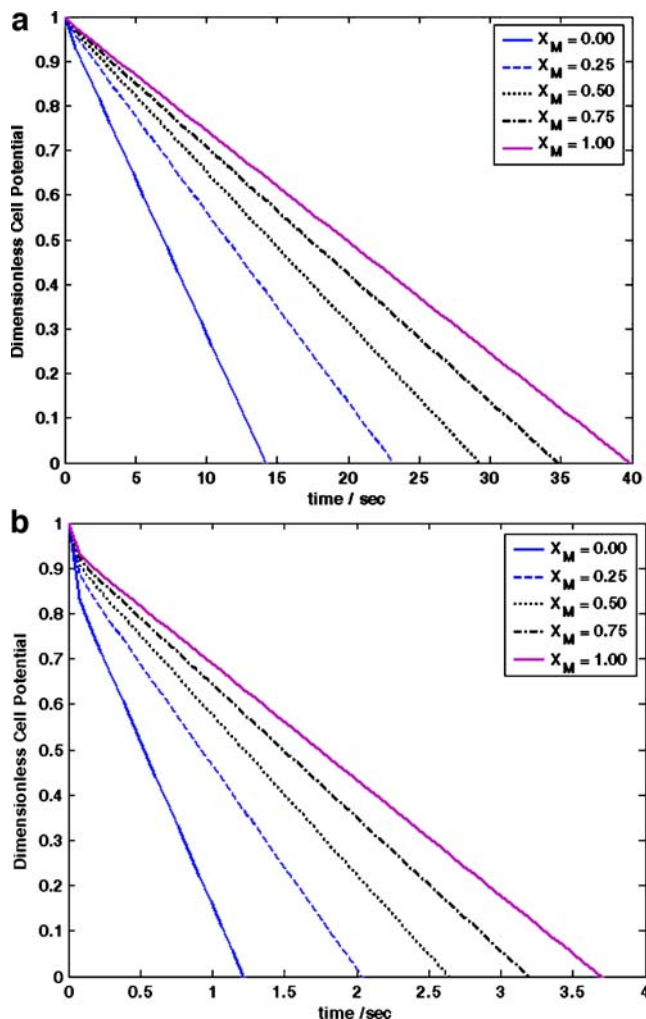

Fig. 3 Discharge curves for a set of pseudocapacitors consisting of 5- and 15-nm RuO_2 nanoparticles with $i_0 = 1 \times 10^{-5} A\, cm^{-2}$ and h=0.4 nm at a 0.05 A and b 0.5 A. X_M shows the volume fraction of 5-nm particles

tered when higher currents are drawn. Another significant characteristic is the dependency of slopes on the composition, which runs in opposite direction. In both capacitor series, the region of slope change shifts to lower potentials (higher potential drops) as the contribution of larger particles increase. The potential fall at the initial discharge times has two origins: ohmic drop (the third term on the right hand side of Eq. 39) and faradaic kinetics resistance [29, 31]. According to Eq. 39, it is expected that the ohmic drop increases as higher currents are withdrawn. Furthermore, decreasing the particles size the ohmic drop decreases because the contact areas have been increased. When the electrochemistry (faradaic reaction) cannot provide the necessary charge (per unit time) to furnish the current cell, the kinetic resistance will be determined. In the present case, when the contribution of smaller particles increases, the total number of active sites and, consequently, the total available charge increase too. The higher the total
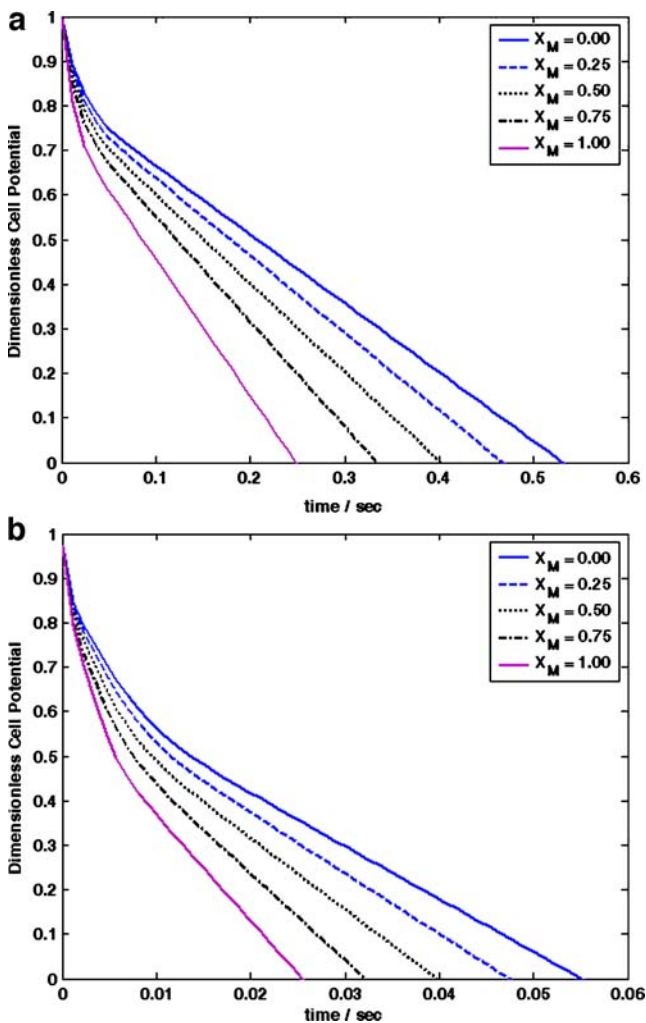
Fig. 4 Discharge curves for a set of pseudocapacitors consisting of 30- and 15-nm RuO$_2$ nanoparticles with $i_0 = 1 \times 10^{-5} A\, cm^{-2}$ and h= 0.4 nm at **a** 0.5 A and **b** 5 A. X_M shows the volume fraction of 30-nm particles

available charge, the lower the kinetic resistance. Table 2 presents the total amount of the charge stored in the capacitor and extracted until the cell potential drops to zero for the active material having X_M fraction of MO$_2$ with d_M of 30 and 5 nm as derived through Eq. 43. The total accessible amount of charge is certainly independent of cell current. In general, the results indicate that the total available charge increases as the contribution of smaller particles increases, which is in line with the expectations. Figure 5 presents the changes of the available charge, $i_{cell}t$, with the composition of electrode (volume fraction of one of the uniformly sized constituents) for a set of supercapacitor consisting of 5- and 15-nm-sized RuO$_2\cdot x$H$_2$O nanoparticles at various cell's current. Figure 6 presents the same data for a supercapacitor consisting 15- and 30-nm-sized RuO$_2\cdot x$H$_2$O particles. In all cases, the amount of the available charge decreases upon increasing the cell current,

Table 1 Model parameters that describe the electrodes and separator

Parameter	Value	Reference
d_{Ru}	15 nm	Assumed
d_M	5 and 30 nm	Assumed
E	0.25	Assumed
ε_S	0.7	Pillay and Newman [38]
$L=L_+=L_-$	5×10^{-3} cm	Assumed
L_S	2.5×10^{-3} cm	Assumed
h_{Ru}	4.0×10^{-8} cm	Pollak and O'Grady [39]
i_0	1×10^{-5} A cm^{-2}	Assumed
Σ	1×10^5 S/cm	Trasatti and Lodi [40]
κ_0	0.8 S/cm	Darling [41]
T	298.15 K	Assumed
V_0	0.5 V (vs. SCE)	Assumed
U_{Ru} (positive electrode)	$0.5\,(1+\theta_{Ru})$ V (vs. SCE)	Jow and Zheng [3]
U_M (positive electrode)	$0.5\,(1+\theta_M)$ V (vs. SCE)	Jow and Zheng [3]
U_{Ru} (negative electrode)	$0.5\theta_{Ru}$ V (vs. SCE)	Assumed
U_M (negative electrode)	$0.5\theta_M$ V (vs. SCE)	Assumed

and the trend reported in Table 2 is reproduced. Furthermore, it is observed that increasing the content of larger particles diminishes the extent of the available charge that is in perfect agreement with the arguments on the effects of surface area and porosity. It seems that, in some cases, there is not much charge available to be withdrawn and, sometimes, although the charge is on the surface, the electrochemistry is not fast enough to make it available to the demand.

To examine how potential, double layer, and faradaic currents inside the electrode change during galvanic discharging, the distribution of potential and the currents as a function of X_M at a specific discharge time was investigated. Figure 7a–c depicts dimensionless localized potential, double layer, and faradaic currents inside the positive electrode for a set of supercapacitors that have different volume fractions of 5- and 15-nm particles of

Table 2 The total available charges in the two series of simulated pseudocapacitors

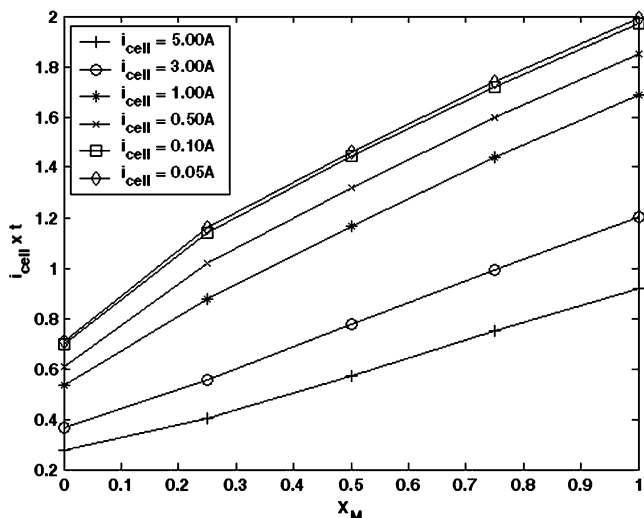| X_M	C_{total} (d_M=30 nm)	C_{total} (d_M=5 nm)
0.00	0.75	0.75
0.25	0.67	1.30
0.50	0.59	1.65
0.75	0.51	1.97
1.00	0.38	2.25

Fig. 5 Available charge, $i_{cell}t$, versus volume fraction of 5-nm particles in a composite electrode for a set of pseudocapacitors consisting of 5- and 15-nm RuO$_2$ nanoparticles with $i_0 = 1 \times 10^{-5} A\,cm^{-2}$ and h=0.4 nm at different withdrawing cell current, which have been shown in the legend. X_M shows the volume fraction of 5-nm particles

RuO$_2$ at a current of 5 A and discharging time of 0.025 s. It should be pointed out that, with $\frac{\partial \theta}{\partial \xi} = 0$, it means there will be no changes of θ inside the electrode. As Fig. 7a illustrates, dimensionless local potential decreases from the current collector surface, ξ=0, to the electrode–electrolyte interface, ξ=1. This behavior is the characteristic of the discharge process. Furthermore, by increasing the volume fraction of 5-nm particles, the smaller particles, the local potential value increases too. This is due to the higher
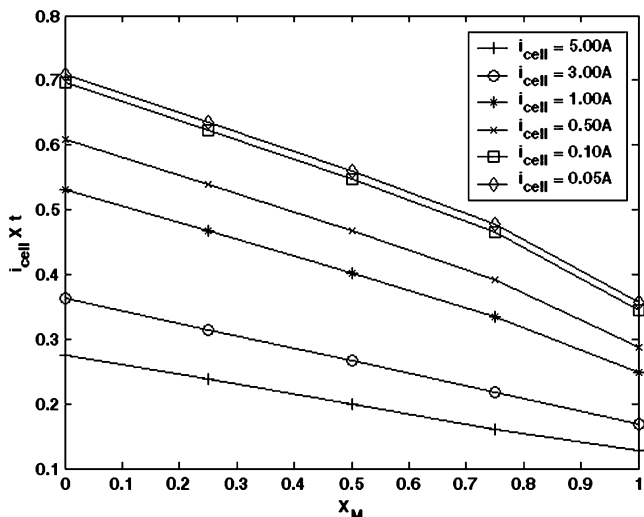

Fig. 6 Available charge, $i_{cell}t$, versus volume fraction of 30-nm particles in a composite electrode for a set of pseudocapacitors consisting of 30- and 15-nm RuO$_2$ nanoparticles with $i_0 = 1 \times 10^{-5} A\,cm^{-2}$ and h=0.4 nm at different withdrawing cell current, which have been shown in the legend. X_M shows the volume fraction of 30-nm particles
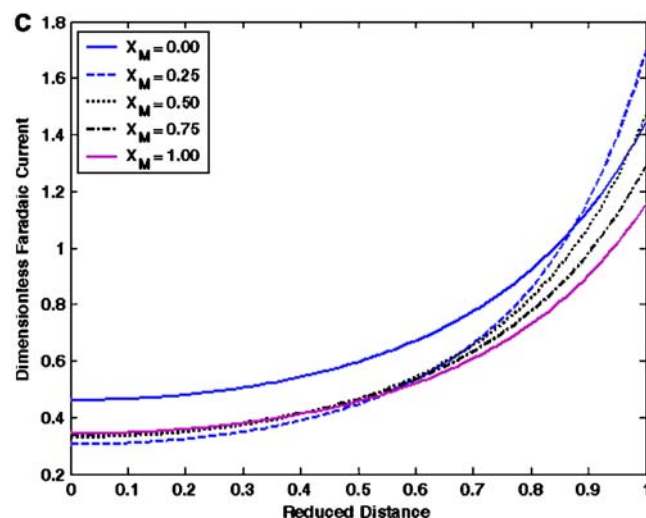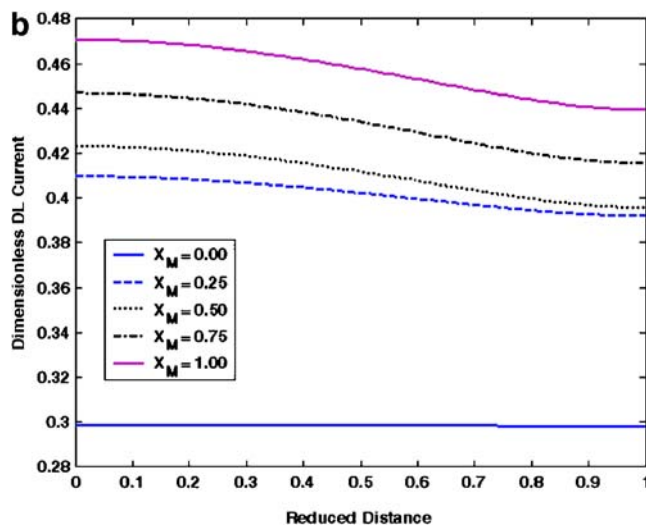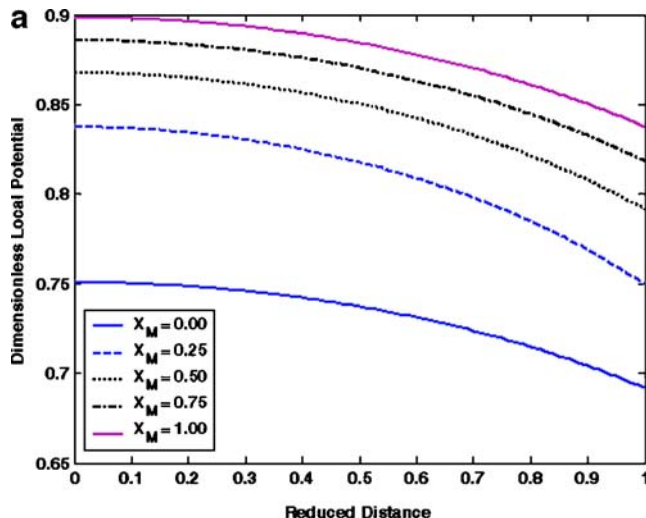

Fig. 7 Distribution of **a** local potential, **b** DL current, and **c** faradaic current inside the positive electrode for a set of pseudocapacitors consisting of 5- and 15-nm RuO$_2$ nanoparticles with $i_0 = 1 \times 10^{-5} A\,cm^{-2}$ and h=0.4 nm at i_{cell}=5 A and t_d=0.025 s. X_M shows the volume fraction of 5-nm particles

Fig. 8 **a** Surface coverage, **b** local potential, **c** DL current, and **d** faradaic current profiles on the surface of positive electrode for a set of pseudocapacitors consisting of 5- and 15-nm RuO$_2$ nanoparticles with $i_0 = 1 \times 10^{-5} A\,cm^{-2}$ and h=0.4 nm at different cell current and X_M. X_M shows the volume fraction of 5-nm particles
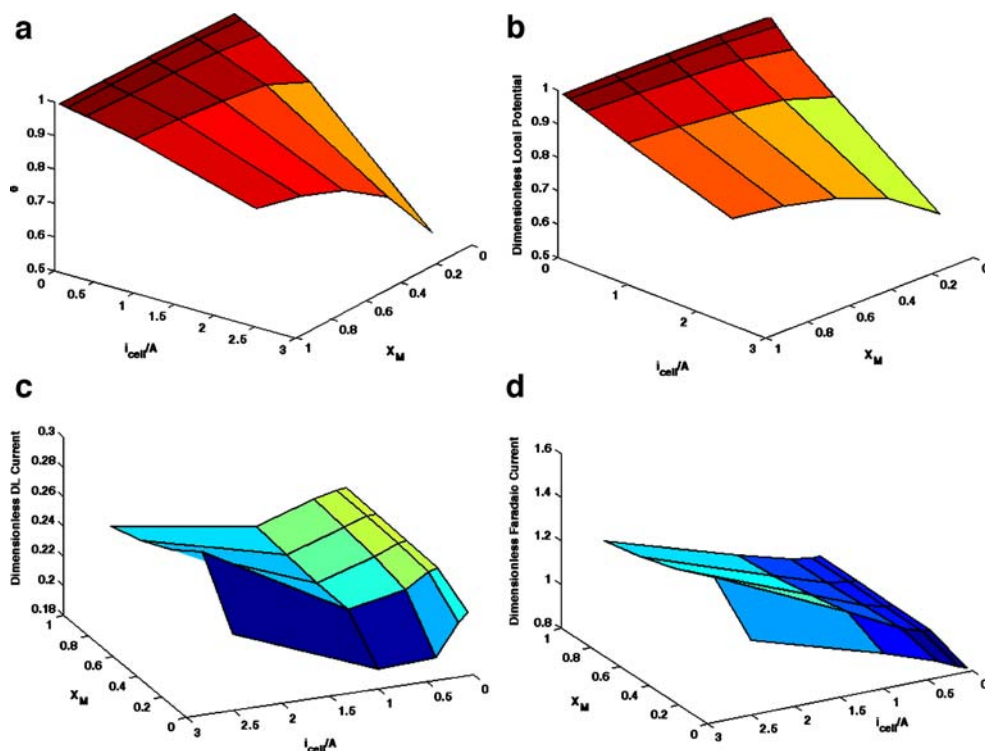
surface area, and so the larger number of active sites presents for large X_M values. The higher the number of active sites, the smaller the θ and E changes. Both double layer charging/discharging and faradaic processes are surface phenomena, which take place at the interface between the electrode and electrolyte. For both of them, more S_V gives rise to more currents, but their distribution inside the electrode will show a different behavior because of their different dependencies to E (Eqs. 40 and 41). Figure 7b illustrates the double layer current profile inside the electrode at various X_M values. For all X_M's, it shows a nonuniform distribution unless X_M=0. The nonuniformity in double layer current distribution depends on double layer time constant (Eq. 25). A discharge time smaller than the double layer time constant predicts a nonuniformity because, in this special case, double layer needs more time to discharge. However, the faradaic current shows a nonuniform and exponential trend (Eqs. 6, 7, and 41), as shown in Fig. 7c. In addition, faradaic currents are larger than double layer current (around four times). It means that the faradaic process has a larger contribution in i_2 compared to the double layer charging process under these conditions.

The contributions of the dimensionless faradaic and double layer discharge currents along with the dimensionless local potential and at various i_{cell} and X_M values are presented in Fig. 8a–d. According to Fig. 8a, the oxidized fraction of particles decreases by increasing the cell current and volume fraction of larger particles. In fact, the total number of available sites for electrodic processes rises by

increasing the volume fraction of smaller nanoparticles. At constant i_{cell}, this is due to increased S_V that causes a smaller fall in the fraction of the sites involved in electrode processes. Consequently, a smaller deviation is observed in θ compared to its initial value at a specified and fixed discharge time. Furthermore, at a constant X_M, more sites get involved in electrodic processes to provide larger current, and so, θ values decrease sharply. The dimensionless local potential variation is parallel to θ changes (see
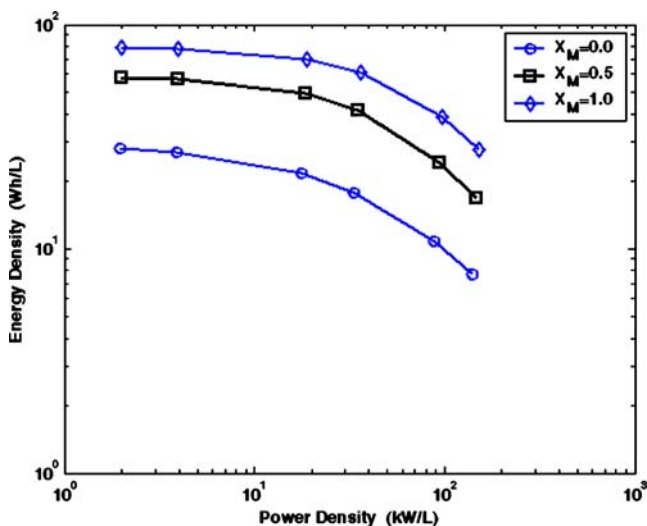

Fig. 9 Ragone plots for a three pseudocapacitors consisting of 5 and 15 nm RuO$_2$ nanoparticles with $i_0 = 1 \times 10^{-5} A\,cm^{-2}$ and h=0.4 nm and different X_M, which have been shown in the legend. X_M shows the volume fraction of 5-nm particles

Fig. 8b); that is, the less the sites involved, the less the changes in dimensionless local potential. Figure 8c and d shows the dimensionless DL and faradaic current variations on the surface of the electrode with cell current and volume fraction of 5-nm particles. Dimensionless DL current decreases by increasing i_{cell} for all X_M values at $i_{cell} < 1$ A, while dimensionless faradaic current increases and it seems that a compensation effect is in operation [31]. However, both DL and faradaic currents rise by increasing the cell current at $i_{cell} < 1$ A. One should remember that, under these conditions, ohmic drop and kinetic resistance govern the potential and, consequently, the behavior of the super-capacitor because electrochemistry cannot provide such large currents and i_1 has, then, a larger contribution in i_{cell} compared to i_2.

Figure 9 presents the Ragone plots for three capacitors having the same i_0 and d_{Ru} with different volume fractions of 5-nm-sized particles. Ragone plots present the variation of energy density with power density for a general power source, and, in the present study, these quantities are calculated through:

$$\text{Energy density} = \frac{i_{cell}\varphi_{ave}t_d}{(2L + L_S)} \quad (44)$$

$$\text{Power density} = \frac{i_{cell}\varphi_{ave}}{(2L + L_S)} \quad (45)$$

$$\varphi_{ave} = \frac{1}{t_d}\int_0^{t_d}\Phi_{cell}dt \quad (46)$$

where t_d is the discharge time and φ_{ave} is the average cell potential in the course of discharge with L and L_S being the electrode's and separator's thicknesses. At first glance, it seems that both power density and energy density increase by increasing cell current, but energy density depends on discharge time too, which decreases by rising the cell current. The overall effect is that the energy density reduces with increasing power density. The high-energy side of the plot corresponds to the faradaic discharge, while the high power end signifies the double layer discharge behavior. At a specified power density, increasing the contribution of large particles decreases the energy density because of the decreasing the number of available sites for the surface faradaic reactions 1 and 2.

Conclusion

A mathematical model of a mixed oxide electrochemical supercapacitor comprising of $RuO_2 \cdot xH_2O$ and $MO_2 \cdot yH_2O$, which MO_2 represents a metal oxide that shows capacitive behavior, was developed. Both double layer and faradaic processes were considered, and the response of the capacitor under galvanostatic charge/discharge conditions was predicted. At this part of the study, M was assumed to chemically behave as Ru, and the effects of particle size distribution and the volume fractions of differently sized particles in DL and faradaic currents, discharge behavior, and power and energy densities of the model capacitor were studied.

References

1. Conway BE (1999) Electrochemical supercapacitors: scientific fundamentals and technological applications. Kluwer, New York
2. Zheng JP, Cygan PJ, Jow TR (1995) J Electrochem Soc 142:2699
3. Jow TR, Zheng JP (1998) J Electrochem Soc 145:49
4. Hu CC, Chen WC (2004) Electrochim Acta 49:3469
5. Sugimoto W, Iwata H, Yokoshima K, Murakami Y, Takasu Y (2005) J Phys Chem B 109:7330
6. Juodkazis K, Juodkazytė J, Šukienė V, Grigucevičienė A, Selskis A (2007) On the charge storage mechanism at $RuO_2/0.5$ M H_2SO_4 interface. J Solid State Electrochem. DOI 10.1007/s10008-007-0476-0
7. Hu CC, Wang CC (2003) J Electrochem Soc 150:A1079
8. Prasad KR, Miura N (2004) J Power Sources 135:354
9. Chen YS, Hu CC, Wu YT (2004) J Solid State Electrochem 8:467
10. Zolfaghari A, Ataherian F, Ghaemi M, Gholami A (2007) Electrochim Acta 52:2806
11. Liu KC, Anderson MA (1996) J Electrochem Soc 143:124
12. Lin C, Ritter JA, Popov BN (1998) J Electrochem Soc 145:4097
13. Xu MW, Bao SJ, Li HL (2007) J Solid State Electrochem 11:372
14. Yong-gang W, Xiao-gang Z (2004) Electrochim Acta 49:1957
15. Liu XM, Zhang XG (2004) Electrochim Acta 49:229
16. Kuo SL, Wu NL (2003) Electrochem Solid-State Lett 6:A85
17. Jeong YU, Manthiram A (2000) Electrochem Solid-State Lett 3:205
18. Chen YS, Hu CC (2003) Electrochem Solid-State Lett 6:A210
19. Prasad KR, Miura N (2004) Electrochemistry Communications 6:1004
20. Nakayama M, Tanaka A, Sato Y, Tonosaki T, Ogura K (2005) Langmuir 21:5907
21. Kuan-Xin H, Quan-Fu W, Xiao-Gang Z (2006) J Electrochem Soc 153:A1568
22. Liang YY, Bao SJ, Li HL (2007) J Solid State Electrochem 11:571
23. Tao F, Shen Y, Liang Y, Li H (2007) J Solid State Electrochem 11:853
24. Zhao Y, Liu L, Xu J, Yanh J, Yan M, Jiang Z (2007) J Solid State Electrochem 11:283
25. Su LH, Zhang XG, Liu Y (2007) Electrochemical performance of Co–Al layered double hydroxide nanosheets mixed with multiwall carbon nanotubes. J Solid State Electrochem. DOI 10.1007/s10008-007-0455-5
26. Wang Y, Yuan A, Wang X (2007) Pseudocapacitive behaviors of nanostructured manganese dioxide/carbon nanotubes composite electrodes in mild aqueous electrolytes: effects of electrolytes and current collectors. J Solid State Electrochem. DOI 10.1007/s10008-007-0445-7
27. Hong JI, Yeo IH, Paik WK (2001) J Electrochem Soc 148:A156
28. Mallouki M, Tran-Van F, Sarrazin C, Simon P, Daffos B, De A, Chevrot C, Fauvarque JF (2007) J Solid State Electrochem 11:398
29. Lin C, Ritter JA, Popov BN, White RE (1999) J Electrochem Soc 146:3168
30. Lin C, Popov BN, Ploehn HJ (2000) J Electrochem Soc 149:A167

31. Farsi H, Gobal F (2007) J Solid State Electrochem 11:1085
32. Nagarajan GS, Van Zee JW, Spotnitz RM (1998) J Electrochem Soc 145:771
33. Yu AB, Zou RP, Standish N (1996) Ind Eng Chem Res 35:3730
34. Kim H, Popov BN (2003) J Electrochem Soc 150:A1153
35. Newman JS (2004) Electrochemical systems, 3rd edn. Prentice-Hall Inc., New York
36. White RE, Lorimer SE, Dardy R (1983) J Electrochem Soc 130:1123
37. J. W. Evans and P. Kar (2008) Notes on BAND and LISOLV. www.mse.berkeley.edu/Groups/Evans/pritish/BandandLisolvNotes.doc
38. Pillay B, Newman J (1996) J Electrochem Soc 143:3791
39. Pollak FH, O'Grady WE (1985) J Electrochem Soc 132:2385
40. Trasatti S, Lodi G (1980) Properties of conductive transition metal oxides with rutiel-type structure. In: Trasatti S (ed) Electrodes of conductive metalic oxides—part A. Elsevier, New York, pp 301–358
41. Darling HE (1964) J Chem Eng Data 9:421